

Strengthening seasonal marine CO₂ variations due to increasing atmospheric CO₂

Peter Landschützer^{1*}, Nicolas Gruber², Dorothee C. E. Bakker³, Irene Stemmler¹ and Katharina D. Six¹

The increase of atmospheric CO₂ (ref. ¹) has been predicted to impact the seasonal cycle of inorganic carbon in the global ocean^{2,3}, yet the observational evidence to verify this prediction has been missing. Here, using an observation-based product of the oceanic partial pressure of CO₂ (p_{CO_2}) covering the past 34 years, we find that the winter-to-summer difference of the p_{CO_2} has increased on average by $2.2 \pm 0.4 \mu\text{atm}$ per decade from 1982 to 2015 poleward of 10° latitude. This is largely in agreement with the trend expected from thermodynamic considerations. Most of the increase stems from the seasonality of the drivers acting on an increasing oceanic p_{CO_2} caused by the uptake of anthropogenic CO₂ from the atmosphere. In the high latitudes, the concurrent ocean-acidification-induced changes in the buffer capacity of the ocean enhance this effect. This strengthening of the seasonal winter-to-summer difference pushes the global ocean towards critical thresholds earlier, inducing stress to ocean ecosystems and fisheries⁴. Our study provides observational evidence for this strengthening seasonal difference in the oceanic carbon cycle on a global scale, illustrating the inevitable consequences of anthropogenic CO₂ emissions.

The oceanic uptake of anthropogenic CO₂ (refs ^{1,5}) is causing major shifts in the surface ocean inorganic carbon system⁶. These shifts include increasing concentrations of dissolved CO₂, and hence higher p_{CO_2} , but also a reduction of the carbonate ion concentration and pH, and are often collectively referred to as ocean acidification^{4,7}. One of the predicted consequences of these chemical changes is an increase in the seasonal variation of the surface ocean p_{CO_2} (refs ^{2,3,8}). However, this prediction has not been confirmed experimentally by in situ data on a global scale so far. Here, by analysing surface ocean p_{CO_2} observations collected over the past 34 years, we demonstrate that the seasonal p_{CO_2} difference indeed has increased substantially in recent decades, implying stronger stress to organisms that are sensitive to ocean acidification^{3,9}.

Our results are based on a collection of ship and mooring surface ocean p_{CO_2} measurements assembled by the Surface Ocean CO₂ Atlas version 4 (SOCATv4) effort^{10,11}. These measurements were combined with our two-step neural network data interpolation technique, self-organizing map–feed-forward network^{12,13}, to reconstruct changes in surface ocean p_{CO_2} from 1982 to 2015 at monthly intervals and with a spatial resolution of $1^\circ \times 1^\circ$. The seasonal differences of p_{CO_2} were computed by first fitting the interpolated data with a combination of harmonic and polynomial functions and then determining the differences for the January–March means and for the July–September means (see Methods).

Although there exists substantial interannual variability in the strength of the seasonal p_{CO_2} difference, expressed here as the seasonal maximum minus the seasonal minimum, its trend is clearly positive in all extratropical regions ranging between $1.1 \pm 0.3 \mu\text{atm}$ per decade and $2.9 \pm 0.3 \mu\text{atm}$ per decade (Fig. 1) with an average rate of $2.2 \pm 0.4 \mu\text{atm}$ per decade.

The seasonal differences observed at the Hawaiian Ocean Time-series station¹⁴ and at the Hydrostation ‘S’/Bermuda Atlantic Time-series Study site^{15–17}, where measurements are available since 1988 and 1983, respectively, support our estimates. The diagnosed trends of $1.5 \pm 1.1 \mu\text{atm}$ per decade (Hydrostation ‘S’/Bermuda Atlantic Time-series Study) and $3.8 \pm 2.4 \mu\text{atm}$ per decade (Hawaiian Ocean Time-series) are statistically indistinguishable from those inferred from our neural-network-based estimates at these two locations ($1.5 \pm 1.8 \mu\text{atm}$ per decade and $0.2 \pm 1.8 \mu\text{atm}$ per decade, respectively; see Supplementary Information). The uncertainties of these local trends are large, however, largely reflecting the strong year-to-year fluctuations of the seasonal cycle of surface ocean p_{CO_2} at this local scale. Although this prevents a very thorough quantitative validation of our neural-network-based analyses, they nevertheless support our estimate of a rate of increase of $2.3 \pm 0.4 \mu\text{atm}$ per decade in the subtropical band ($10\text{--}40^\circ\text{N}$) of the Northern Hemisphere. This is particularly encouraging considering the local nature of these station data in comparison with our larger-scale self-organizing-map–feed-forward-network estimates. This conclusion is further supported by the residuals of our interpolated product having no seasonal trend, that is, the diagnosed trend in the seasonal difference is not an artefact of the interpolation, but stems from the p_{CO_2} observations (see Supplementary Information). The long-term changes in the winter-minus-summer differences for the large-scale regions analysed here are also considerably larger than the estimated uncertainty in the reconstructed seasonal cycles for p_{CO_2} .

The seasonal differences of the surface p_{CO_2} increase everywhere, with the winter-minus-summer differences becoming more negative in the low latitudes (equatorward of $\sim 40^\circ$), and more positive in the high latitudes (poleward of $\sim 40^\circ$) (Fig. 2). This change in the sign between the low and the high latitudes corresponds to the seasonal maxima of p_{CO_2} being six months out of phase between these two bands (Fig. 2e). In the low latitudes, the seasonal cycle has a maximum in summer, and thus a negative winter-minus-summer difference (Fig. 2a,c). In contrast, the seasonal cycle in the high latitudes has a maximum in winter, leading to a positive winter-minus-summer difference in p_{CO_2} (Fig. 2b,d). For our further analyses, we will use the winter-minus-summer difference rather than

¹Max Planck Institute for Meteorology, Hamburg, Germany. ²Environmental Physics, Institute of Biogeochemistry and Pollutant Dynamics, ETH Zurich, Zurich, Switzerland. ³Centre for Ocean and Atmospheric Sciences, School of Environmental Sciences, University of East Anglia, Norwich, UK.

*e-mail: peter.landschuetzer@mpimet.mpg.de

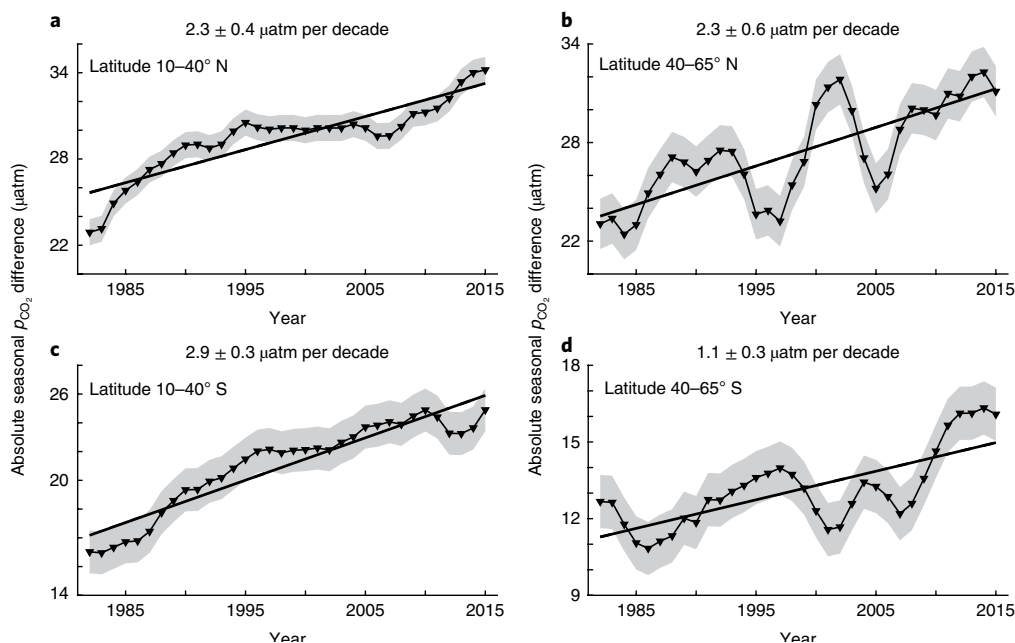


Fig. 1 | Trends in the seasonal difference of sea surface p_{CO_2} 1982-2015 **a**, 10-40° N. **b**, 40-65° N. **c**, 10-40° S. **d**, 40-65° S. Trends are derived from the updated version of an observation-based sea surface p_{CO_2} product¹³. Black markers represent the seasonal maximum minus seasonal minimum for each year, and the solid regression line represents the results of a linear least-squares regression. The shaded area represents the uncertainty calculated as the standard error of the interpolated p_{CO_2} product. The slope of the line, displayed at the top of each panel, represents the trends in seasonal variations, that is, the trend in the seasonal maximum minus the seasonal minimum including its 95% confidence interval.

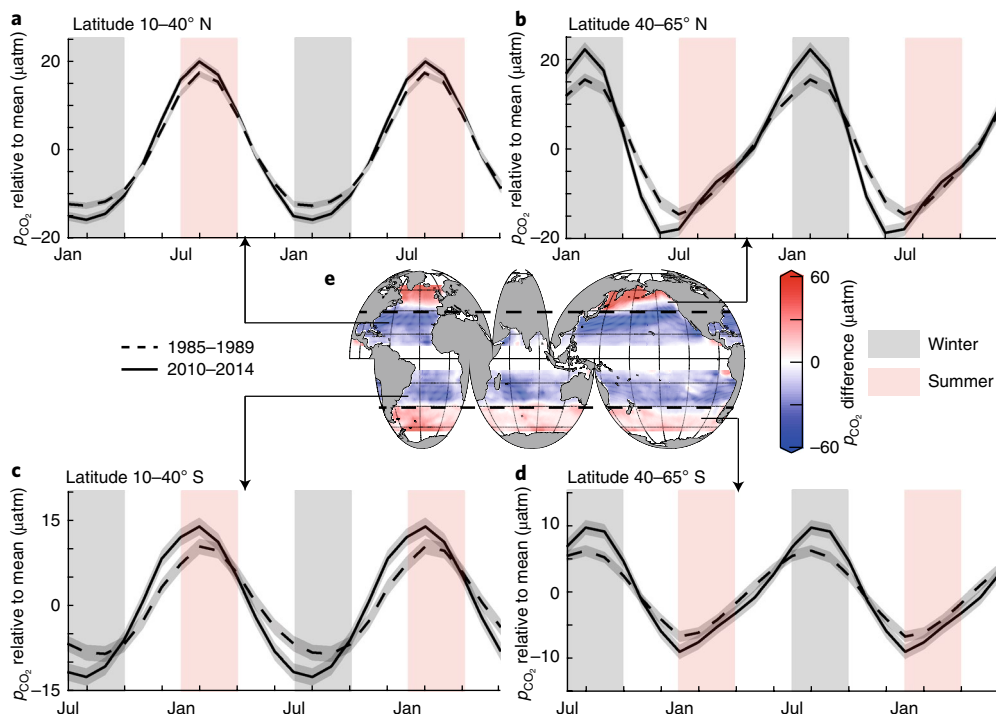


Fig. 2 | The changing seasonal sea surface p_{CO_2} cycle **a**, 10-40° N. **b**, 40-65° N. **c**, 10-40° S. **d**, 40-65° S. Each panel consists of a comparison of the mean seasonal cycle from 1985-1989 (dashed line) and 2010-2014 (solid line) relative to the respective mean p_{CO_2} , including shaded standard error uncertainty estimates. The mean seasonal cycles for each respective period are repeated, and those of the Southern Hemisphere are shifted by six months to align the seasons. **e**, The climatological mean winter-minus-summer difference for each 1°x1° pixel. Positive winter-minus-summer differences are marked in red, whereas negative winter-minus-summer differences are marked in blue.

the absolute difference as our metric for changes in the seasonal cycle, mainly because including the sign permits us to investigate the dominant drivers for the winter-minus-summer trends.

We can quantify these drivers by separating the seasonal cycle of the surface ocean p_{CO_2} into the thermal part driven by the seasonal variations in sea surface temperature (SST) and

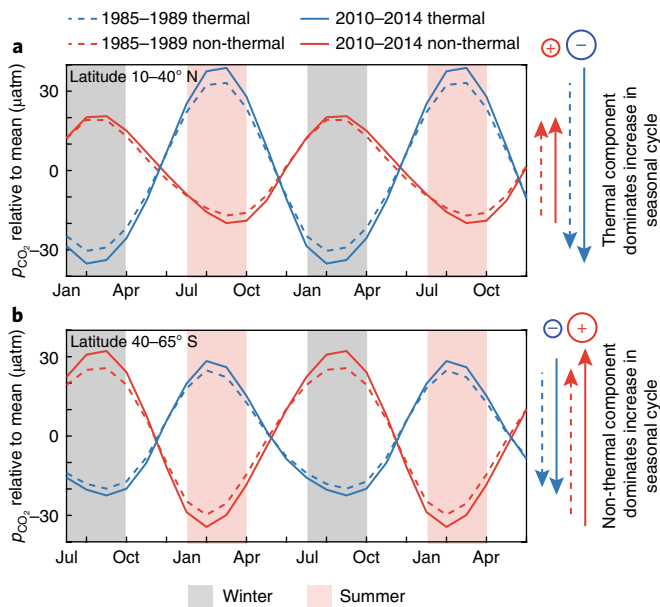


Fig. 3 | Separation of the five-year mean seasonal cycle of p_{CO_2} into its thermal and non-thermal components a, 10–40° N. b, 40–65° S. Shown are the data for the period 1985–1989 (dashed lines) and 2010–2014 (solid lines). While in **a** the non-thermal component increases the seasonal winter-minus-summer difference (marked in red with a plus sign highlighting the positive transition from winter maximum to summer minimum), the opposing thermal signal is stronger, leading to an increase in the summer-minus-winter difference (marked in blue with a minus sign highlighting the negative transition from winter minimum to summer maximum). Vice versa, in **b** the non-thermal component dominates over the thermal component.

into the non-thermal part driven by the seasonal variations by all other factors, namely dissolved inorganic carbon (DIC), alkalinity and salinity^{6,18,19} (Fig. 3). This separation shows that the winter-minus-summer differences of the thermal component became more negative between the periods 1985–1989 and the 2010–2014, while the winter-minus-summer difference in the non-thermal component became more positive between these two periods. While these trends oppose each other, in the low latitudes (Fig. 3a), the negative winter-minus-summer trend in the thermal component dominates the increase in the seasonal p_{CO_2} difference, whereas in the high latitude regions (Fig. 3b), the positive winter-minus-summer trend in the non-thermal component is the dominating component. Consequently, adding both components, we find an increase in the seasonal p_{CO_2} difference everywhere in the global ocean.

The regionally varying contribution of the thermal and non-thermal components to the changing seasonal cycle is also clearly visible in a regionally more refined analysis of the winter-minus-summer trends (Fig. 4), even though the regional winter-minus-summer p_{CO_2} trends vary more substantially than the broad latitude band averages (Fig. 4a). Trends in the winter-minus-summer p_{CO_2} difference of the thermal and non-thermal components are locally even stronger, reaching 10 μatm per decade, but the compensatory nature of the thermal and non-thermal trend components occurs nearly everywhere (Fig. 4b,c).

Thermodynamic consideration of the CO_2 system in seawater permits us to determine and quantify the drivers behind the increases in the seasonal differences as well as the compensatory nature between the thermal and non-thermal components. Starting from a Taylor expansion of the p_{CO_2} drivers^{6,18}, and using some

simplifications, we can show that three mechanisms are driving the increase in the seasonal differences (see Methods). The first mechanism is associated with the long-term increase in the mean concentration of CO_2 in the surface ocean, $[\text{CO}_2]_{\text{aq}}$, caused by the uptake of anthropogenic CO_2 from the atmosphere. This mechanism affects both the thermal and non-thermal driven seasonal cycle because of their respective CO_2 sensitivities. The second mechanism is associated with the reaction of the added CO_2 with the carbonate ion in seawater, resulting in a reduction of the capacity of the surface ocean CO_2 system to buffer against changes. This consequence, reflected in an increase in the Revelle (buffer) factor, implies that the surface ocean CO_2 system becomes more sensitive to the seasonal cycle in DIC and alkalinity³. The third mechanism changes the seasonal p_{CO_2} difference by altering the seasonality of its drivers.

We do not have sufficient long-term observations of surface DIC, alkalinity and salinity to determine the changes in their seasonal cycles required to estimate quantitatively the contribution of the third mechanism. In response, we investigate how much of the observed trends can be attributed to the increase in the CO_2 concentration and buffer factor, and then discuss the role of the third mechanism based on the mismatch between the observations and the estimates from the first two mechanisms.

The comparison between our observation-based winter-minus-summer trends and those from the thermodynamic consideration (dashed green lines in Fig. 4) illustrates that the first two mechanisms can explain most of the observation-based latitudinal trend pattern. This indicates that the contribution of the third mechanism, namely changes in the seasonality of the p_{CO_2} drivers, is comparably small. The dominance of the first two mechanisms implies that it is indeed the long-term changes in the surface ocean CO_2 chemistry linked to the increasing uptake of anthropogenic CO_2 that cause the increase in the winter-minus-summer difference in surface ocean p_{CO_2} , confirming model-based analyses^{2,3,20}.

Further details emerge when the thermal and the non-thermal p_{CO_2} components are considered separately (Fig. 4b,c). In particular, this analysis allows us to explain why the thermal and non-thermal components drive the change in the low and high latitudes, respectively. As it turns out, this is the result of the increasing oceanic CO_2 concentration being responsible for roughly two-thirds of the predicted trend in the non-thermal component and for all of the predicted trend in the thermal component (see Supplementary Fig. 8). This dominance results in this driver enhancing both components in roughly equal manner, but because these two components have opposing seasonality, the net effect depends on which component dominates the seasonal cycle. As a result, in regions where the seasonal cycle of p_{CO_2} is dominated by the thermal component, the trend in the winter-minus-summer difference is dominated by this component as well. In an analogous manner, the non-thermal component drives both the seasonal cycle and the trend in the winter-minus-summer difference in the high latitudes.

While the consideration of the first two mechanisms explains most of the observed trends, there are also substantial differences, implying changes in the seasonality of the p_{CO_2} drivers. Figure 4 shows that the underestimation of the winter-minus-summer trend in the low and temperate latitudes of the Northern Hemisphere stems from an underestimation of the thermal component (Fig. 4b). This implies that a trend towards a stronger seasonal warming of the sea surface contributed to the larger seasonal difference in p_{CO_2} as well. In contrast, the underestimation of the observation-based trend in the low and temperate latitudes of the Southern Hemisphere (Fig. 4a) stems primarily from the non-thermal p_{CO_2} component (Fig. 4c). This implies that a reduction or shift of the seasonal cycle of DIC, or an increase in the seasonal cycle of alkalinity, contributed to the weaker increase of the winter-minus-summer difference. A plausible cause is natural variability of the

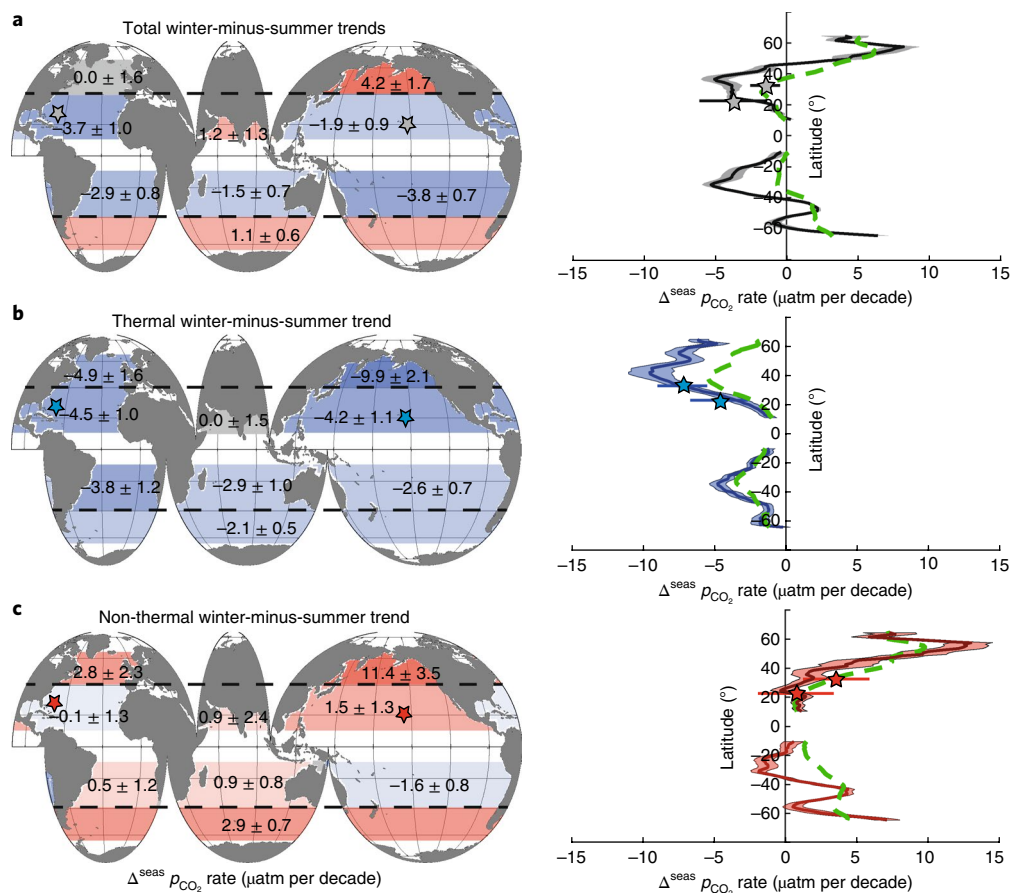


Fig. 4 | Regional and zonal mean trends in the winter-minus-summer difference. **a–c**, Total (**a**), thermal (**b**) and non-thermal (**c**) trends in the seasonal p_{CO_2} cycles visualized both geographically (left) and as zonal means (right, by black, blue and red lines, respectively). Coloured regions on the left represent positive (red) and negative (blue) winter minus summer p_{CO_2} trends whereas the shading represents the strength of the trends, that is, light colours represent weaker trends and darker colours represent stronger trends. Negative trends highlight an increasing summer maximum and decreasing winter minimum, whereas positive trends highlight increasing winter maxima and decreasing summer minima. The dashed green lines represent the expected increase based on our thermodynamic consideration considering only the effect of the increase in surface ocean CO_2 and changes in Revelle factor (see main text). Stars further indicate the observation-based (grey, blue, red) winter-minus-summer trends from time series stations at Bermuda and Hawaii. Note that the stars are trends at a single location, while the trends shown based on the neural-network-based p_{CO_2} analyses represent basin-scale or global zonal mean trends.

surface ocean p_{CO_2} in the subtropical Pacific in response to El Niño/Southern Oscillation. The decadal-scale variability of the Southern Ocean carbon sink^{21,22} may matter as well, particularly since a weaker seasonal cycle of DIC would be consistent with recent estimates indicating a weaker accumulation of CO_2 in the surface waters of the Southern Ocean²² linked to changes in the shallow overturning circulation²³. This mismatch in the non-thermal seasonal difference trends, however, might also reflect our limitation to estimate seasonal trends in the austral winter because of the limited amount of seasonal CO_2 measurements²⁴.

Our ability to verify experimentally the increase in the seasonal variations of the surface ocean p_{CO_2} is encouraging. It demonstrates the great advances of the surface ocean observation networks and their interpretation through various interpolation schemes^{11,25}. Our finding that most of the increase in the seasonal winter-minus-summer difference is driven by the rise in atmospheric CO_2 implies that this increase should be a robust feature across different models and observations, as it does not depend on the magnitude of climate change and on any feedbacks between climate and the ocean carbon cycle.

The increase in the seasonal difference of the surface ocean p_{CO_2} enhances in a substantial manner the effects of ocean

acidification^{4,26,27} on marine organisms, as they are exposed earlier to higher levels of ocean acidification, possibly inducing the transition across critical thresholds harmful to ocean ecosystems and fisheries, such as hypercapnia and low saturation states with regard to calcium carbonate^{3,9,28}. Additionally, the observation-based trends are subject to substantial natural climate variability, and the full extent of the seasonal p_{CO_2} difference is probably still masked²⁹. This circumstance does not allow us to distinguish fully between decadal-scale climate variability and anthropogenic trends, a difference that can be resolved by only long-term observational records. Our observation-based study, however, shows that anthropogenic CO_2 emissions have already left a detectable imprint on the marine carbon cycle in the form of an increasing seasonal difference of the surface ocean CO_2 over the past decades.

Methods

Methods, including statements of data availability and any associated accession codes and references, are available at <https://doi.org/10.1038/s41558-017-0057-x>.

Received: 27 June 2017; Accepted: 12 December 2017; Published online: 29 January 2018

References

1. Le Quéré, C. et al. Global carbon budget 2016. *Earth Syst. Sci. Data* **8**, 605–649 (2016).
2. Rodgers, K. B. et al. A wintertime uptake window for anthropogenic CO₂ in the North Pacific. *Glob. Biogeochem. Cycles* **22**, GB2020 (2008).
3. Hauck, J. & Völker, C. Rising atmospheric CO₂ leads to large impact of biology on Southern Ocean CO₂ uptake via changes of the Revelle factor. *Geophys. Res. Lett.* **42**, 1459–1464 (2015).
4. Doney, S., Fabry, V., Feely, R. A. & Kleypas, J. Ocean acidification: the other CO₂ problem. *Annu. Rev. Mar. Sci.* **1**, 169–192 (2009).
5. Sarmiento, J. M. et al. Trends and regional distributions of land and ocean carbon sinks. *Biogeosciences* **7**, 2351–2367 (2010).
6. Sarmiento, J. & Gruber, N. *Ocean Biogeochemical Dynamics* (Princeton Univ. Press, New Jersey, 2006).
7. Orr, J. C. et al. Anthropogenic ocean acidification over the twenty-first century and its impact on calcifying organisms. *Nature* **437**, 681–686 (2005).
8. Delille, B. et al. Response of primary production and calcification to changes of pCO₂ during experimental blooms of the coccolithophorid *Emiliania huxleyi*. *Glob. Biogeochem. Cycles* **19**, GB2023 (2005).
9. McNeil, B. I. & Sasse, T. P. Future ocean hypercapnia driven by anthropogenic amplification of the natural CO₂ cycle. *Nature* **529**, 383–386 (2016).
10. Sabine, C. L. et al. Surface Ocean CO₂ Atlas (SOCAT) gridded data products. *Earth Syst. Sci. Data* **5**, 145–153 (2013).
11. Bakker, D. C. E. et al. A multi-decade record of high-quality fCO₂ data in version 3 of the Surface Ocean CO₂ Atlas (SOCAT). *Earth Syst. Sci. Data* **8**, 383–413 (2016).
12. Landschützer, P. et al. A neural network-based estimate of the seasonal to inter-annual variability of the Atlantic Ocean carbon sink. *Biogeosciences* **10**, 7793–7815 (2013).
13. Landschützer, P., Gruber, N. & Bakker, D. C. E. Decadal variations and trends of the global ocean carbon sink. *Glob. Biogeochem. Cycles* **30**, 1396–1417 (2016).
14. Dore, J. E., Lukas, R., Sadler, D. W., Church, M. J. & Karl, D. M. Physical and biogeochemical modulation of ocean acidification in the central North Pacific. *Proc. Natl. Acad. Sci. USA* **106**, 12235–12240 (2009).
15. Gruber, N., Keeling, C. D. & Bates, N. R. Interannual variability in the North Atlantic Ocean carbon sink. *Science* **298**, 2374–2378 (2002).
16. Bates, N. R. Multi-decadal uptake of carbon dioxide into subtropical mode water of the North Atlantic Ocean. *Biogeosciences* **9**, 2649–2659 (2012).
17. Phillips, H. E. & Joyce, T. M. Bermuda's tale of two time series: Hydrostation 'S' and BATS. *J. Phys. Oceanogr.* **37**, 554–571 (2006).
18. Takahashi, T., Olafsson, J., Goddard, J., Chipman, D. & Sutherland, S. Seasonal variation of CO₂ and nutrients in the high-latitude surface oceans: a comparative study. *Glob. Biogeochem. Cycles* **7**, 843–878 (1993).
19. Takahashi, T. et al. Global sea-air CO₂ flux based on climatological surface ocean pCO₂, and seasonal biological and temperature effects. *Deep-Sea Res. II* **49**, 1601–1622 (2002).
20. Gorgues, T., Aumont, O. & Rodgers, K. B. A mechanistic account of increasing seasonal variations in the rate of ocean uptake of anthropogenic carbon. *Biogeosciences* **7**, 2581–2589 (2010).
21. Le Quéré, C. et al. Saturation of the Southern Ocean CO₂ sink due to recent climate change. *Science* **316**, 1735–1738 (2007).
22. Landschützer, P. et al. The reinvigoration of the Southern Ocean carbon sink. *Science* **349**, 1221–1224 (2015).
23. DeVries, T., Holzer, M. & Primeau, F. Recent increase in oceanic carbon uptake driven by weaker upper-ocean overturning. *Nature* **542**, 215–218 (2017).
24. Monteiro, P. M. S. et al. Intraseasonal variability linked to sampling alias in air-sea CO₂ fluxes in the Southern Ocean. *Geophys. Res. Lett.* **42**, 8507–8514 (2015).
25. Rödenbeck, C. et al. Data-based estimates of the ocean carbon sink variability—first results of the Surface Ocean pCO₂ Mapping intercomparison (SOCOM). *Biogeosciences* **12**, 7251–7278 (2015).
26. Bates, N. et al. A time-series view of changing ocean chemistry due to ocean uptake of anthropogenic CO₂ and ocean acidification. *Oceanography* **27**, 126–141 (2014).
27. Lauvset, S. K., Gruber, N., Landschützer, P., Olsen, A. & Tjiputra, J. Trends and drivers in global surface ocean pH over the past 3 decades. *Biogeosciences* **12**, 1285–1298 (2015).
28. Gruber, N. et al. Rapid progression of ocean acidification in the California Current System. *Science* **337**, 220–223 (2012).
29. McKinley, G. A. et al. Timescales for detection of trends in the ocean carbon sink. *Nature* **530**, 469–472 (2016).

Acknowledgements

We thank J. Marotzke and H. Li from the Max Planck Institute for Meteorology in Hamburg for their comments. P.L. was supported by the Max Planck Society for the Advancement of Science. N.G. was supported by ETH Zürich (Swiss Federal Institute of Technology in Zürich) and by European Union grant 283080 (GEOCARBON). D.C.E.B. was supported by the United Kingdom Shelf Sea Biogeochemistry Blue Carbon project (NE/K00168X/1; funded by the Natural Environment Research Council, the Department for Energy and Climate Change and the Department for Environment, Food and Rural Affairs). K.D.S. was partly supported through the Cluster of Excellence 'CliSAP' (EXC177), University of Hamburg, funded through the German Research Foundation (DFG).

Author contributions

P.L. and N.G. designed the study with input from D.C.E.B. N.G. and P.L. developed the theoretical framework and wrote the paper together with D.C.E.B., I.S. and K.D.S. P.L. developed the neural network method and performed the analysis, assisted by N.G., I.S. and K.D.S. D.C.E.B. led the SOCAT synthesis effort that underlies this work. All authors discussed the results and implications and commented on the manuscript at all stages.

Competing interests

The authors declare no competing financial interests.

Additional information

Supplementary information is available for this paper at <https://doi.org/10.1038/s41558-017-0057-x>.

Reprints and permissions information is available at www.nature.com/reprints.

Correspondence and requests for materials should be addressed to P.L.

Publisher's note: Springer Nature remains neutral with regard to jurisdictional claims in published maps and institutional affiliations.

Methods

Calculation of the seasonal differences and trends. To compute the winter-minus-summer differences of our p_{CO_2} product, we first fit a third-order polynomial (to account for trends) and fourth-order harmonic function (to reproduce the seasonality) to all data to reproduce the full seasonal cycle³⁰

$$f(t) = a_1 + a_2 \times t + a_3 \times t^2 + a_4 \times \sin(2 \times \pi \times t/T) + a_5 \times \cos(2 \times \pi \times t/T) + a_6 \times \sin(4 \times \pi \times t/T) + a_7 \times \cos(4 \times \pi \times t/T) \quad (1)$$

where t is time in years and T is the period, chosen here as 1 yr.

We recreate the seasonal cycle of a certain year by fitting equation (1) to every full analysis year, as well as the year before and after that, creating three-year running time series. Years at the beginning or the end of our time series are reconstructed using the two following or preceding years.

From the resulting harmonic function $f(t)$ segments, we calculate winter averages in the Northern Hemisphere as the mean of the months January, February and March, and summer averages as the mean of the months July, August and September, and vice versa for the Southern Hemisphere. The seasonal maximum minus seasonal minimum for a certain year is then calculated as the difference between winter-minus-summer means.

Trends in these winter-minus-summer differences are then calculated from the slope of the linear regression line fit to the 34-year time series, and uncertainties are derived from the t -statistic of the regression (see below). We repeated our analysis without the quadratic ($a_3 \times t^2$) and linear terms ($a_2 \times t$) in equation (1), but find only small difference between the estimated cycles and seasonal trends (not shown).

Calculation of thermal and non-thermal components. We split the observation-based p_{CO_2} into its thermal (superscript 'th') and non-thermal (superscript 'nt') components, that is, that part driven by the seasonal variations in SST, and that part driven by the seasonal variations by all other factors, namely DIC, alkalinity and salinity^{18,19}. To compute the thermal component, we use the well-established temperature sensitivity of CO_2 (γ_T) of 4.23%/°C (ref. 19). This experimentally determined sensitivity may divert from the exact local sensitivity, but this error is very small and therefore not further considered. Furthermore, we perturb the annual mean p_{CO_2} $\langle p_{CO_2} \rangle_{\text{annual}}$ with the observed temperature anomalies, that is, the differences between the measured SST and the long-term mean SST, $\langle SST \rangle$:

$$p_{CO_2}^{\text{th}} = \langle p_{CO_2} \rangle_{\text{annual}} \times \exp(\gamma_T \times (SST - \langle SST \rangle)) \quad (2)$$

The non-thermal component is computed by removing the temperature effect from the observation-based p_{CO_2} , while normalizing the p_{CO_2} values to the long-term mean SST, $\langle SST \rangle$ (ref. 19):

$$p_{CO_2}^{\text{nt}} = p_{CO_2} \times \exp(\gamma_T \times (\langle SST \rangle - SST)) \quad (3)$$

Drivers of the seasonal p_{CO_2} difference trends. To determine the potential drivers of the observed trends in the winter-minus-summer differences in p_{CO_2} , we start with a decomposition of any variations in p_{CO_2} into their driving components, namely SST, sea surface salinity (S), DIC and total alkalinity (Alk), thereby neglecting the very small contribution arising from variations in nutrients and other very minor drivers. Considering only the first-order terms of a Taylor expansion gives, for any change in p_{CO_2} , that is, dp_{CO_2} (refs 6,18),

$$dp_{CO_2} = \frac{\partial p_{CO_2}}{\partial SST} \times dSST + \frac{\partial p_{CO_2}}{\partial DIC} \times dDIC + \frac{\partial p_{CO_2}}{\partial Alk} \times dAlk + \frac{\partial p_{CO_2}}{\partial S} \times dS \quad (4)$$

where the 'd' denotes deviations of this property from some norm (with the assumption that 'd' is small relative to mean value). Since variations in the freshwater (FW) input to the surface ocean affect not only salinity but also DIC and Alk (with the last two opposing each other), it is often more insightful to combine all terms affected by freshwater fluxes into one³¹, leaving only the seasonal changes in salinity-normalized DIC and Alk in the respective terms. The salinity normalization is given by $sDIC = S/S_0 \times DIC$, $sAlk = S/S_0 \times Alk$, with S_0 representing the normalization salinity, here taken as the annual mean salinity. This gives

$$dp_{CO_2} = \frac{\partial p_{CO_2}}{\partial SST} \times dSST + \frac{\partial p_{CO_2}}{\partial DIC} \times S/S_0 \times dsDIC + \frac{\partial p_{CO_2}}{\partial Alk} \times S/S_0 \times dsAlk + \frac{\partial p_{CO_2}}{\partial FW} \times dFW \quad (5)$$

The partial derivatives with regard to any of the drivers, that is, ∂p_{CO_2} can be estimated from the p_{CO_2} sensitivities, γ (ref. 6). As we are considering deviations

from the annual mean, S/S_0 is essentially equal to 1 and will be dropped subsequently. Taking advantage of this simplification, inserting these sensitivities and replacing 'd' with the seasonal difference, Δ^{seas} , yields

$$\Delta^{\text{seas}} p_{CO_2} = \frac{\gamma_T \times p_{CO_2} \times \Delta^{\text{seas}} SST}{\text{sensitivity to temperature}} + \frac{\gamma_{DIC} \times \frac{p_{CO_2}}{DIC} \times \Delta^{\text{seas}} sDIC}{\text{sensitivity to sDIC}} + \frac{\gamma_{Alk} \times \frac{p_{CO_2}}{Alk} \times \Delta^{\text{seas}} sAlk}{\text{sensitivity to sAlk}} + \frac{\gamma_{FW} \times \frac{p_{CO_2}}{FW} \times \Delta^{\text{seas}} FW}{\text{sensitivity to freshwater}} \quad (6)$$

where γ_T is the temperature sensitivity (see above), and where $\gamma_{DIC,Alk,FW}$ describe the dimensionless p_{CO_2} sensitivities of the remaining terms, with γ_{DIC} usually referred to as the Revelle factor³².

The first term of the right-hand side of equation (6) represents the seasonal difference of the thermal component, while the remaining three terms of the right-hand side together represent the seasonal difference of the non-thermal component. To simplify the further analysis, we take advantage of the observation that the contribution of sAlk and FW to the seasonal cycle of p_{CO_2} is generally much smaller than that of SST and sDIC (ref. 6). This permits us to drop these terms subsequently. We expect this simplification to work well across most of the ocean basins, where the seasonal changes in sAlk are very small³³, but less so in high latitude and coastal ocean regions, where both the sAlk and the freshwater fluxes are larger. However, since we investigate zonal mean trends and no trends poleward of 65°N and 65°S, respectively, we expect our simplification to work very well. The non-thermal part of equation (6) thus reduces to a single component driven by sDIC:

$$\Delta^{\text{seas}} p_{CO_2} = \Delta^{\text{seas}} p_{CO_2}^{\text{th}} + \Delta^{\text{seas}} p_{CO_2}^{\text{nt}} \approx \gamma_T \times p_{CO_2} \times \Delta^{\text{seas}} SST + \gamma_{sDIC} \times \frac{p_{CO_2}}{DIC} \times \Delta^{\text{seas}} sDIC \quad (7)$$

We next determine the temporal trends in these two components. Computing the temporal derivative of the seasonal difference, we derive

$$\frac{d\Delta^{\text{seas}} p_{CO_2}}{dt} = \gamma_T \times \frac{dp_{CO_2}}{dt} \times \Delta^{\text{seas}} SST + \gamma_T \times p_{CO_2} \times \frac{d\Delta^{\text{seas}} SST}{dt} + \frac{d\gamma_{DIC}}{dt} \times \frac{p_{CO_2}}{DIC} \times \Delta^{\text{seas}} sDIC + \gamma_{DIC} \times \Delta^{\text{seas}} sDIC \times \left(\frac{dp_{CO_2}/dt}{DIC} - dDIC/dt \times \frac{p_{CO_2}}{DIC^2} \right) + \gamma_{DIC} \times \frac{p_{CO_2}}{DIC} \times \frac{d\Delta^{\text{seas}} sDIC}{dt} \quad (8)$$

Since dp_{CO_2}/dt and $dDIC/dt$ are of similar magnitude (long-term mean $dp_{CO_2}/dt \approx 1.5 \text{ } \mu\text{atm yr}^{-1}$), while $p_{CO_2}/DIC \ll 1$, the second term inside the bracket in equation (8) is considerably smaller than the first term. Thus, this equation can be simplified to

$$\frac{d\Delta^{\text{seas}} p_{CO_2}}{dt} = \gamma_T \times \frac{dp_{CO_2}}{dt} \times \Delta^{\text{seas}} SST + \gamma_T \times p_{CO_2} \times \frac{d\Delta^{\text{seas}} SST}{dt} + \frac{d\gamma_{DIC}}{dt} \times \frac{p_{CO_2}}{DIC} \times \Delta^{\text{seas}} sDIC + \gamma_{DIC} \times \frac{dp_{CO_2}}{dt} \times \frac{\Delta^{\text{seas}} sDIC}{DIC} + \gamma_{DIC} \times \frac{p_{CO_2}}{DIC} \times \frac{d\Delta^{\text{seas}} sDIC}{dt} \quad (9)$$

and further

$$\frac{d\Delta^{\text{seas}} p_{CO_2}}{dt} = \frac{\frac{dp_{CO_2}}{dt} \times \left(\gamma_T \times \Delta^{\text{seas}} SST + \gamma_{DIC} \times \frac{\Delta^{\text{seas}} sDIC}{DIC} \right)}{\text{change in surface } p_{CO_2}} + \frac{\frac{d\gamma_{DIC}}{dt} \times \frac{p_{CO_2}}{DIC} \times \Delta^{\text{seas}} sDIC}{\text{Revelle factor change}} + \frac{\frac{d\Delta^{\text{seas}} sDIC}{dt} \times \gamma_{DIC} \times \frac{p_{CO_2}}{DIC} + \frac{d\Delta^{\text{seas}} SST}{dt} \times \gamma_T \times p_{CO_2}}{\text{seasonal difference change}} \quad (10)$$

Analysing the terms that can drive a trend in the winter-minus-summer differences in p_{CO_2} shows that we have three sets of processes to consider. The first one is associated with the long-term change in surface ocean p_{CO_2} . This causes a trend simply by the seasonal variations in SST and sDIC acting on an increasing p_{CO_2} . The second process is a result of ocean acidification causing an increase in the Revelle factor. This term is, like the first one, directly tied to the increase in atmospheric CO_2 driving an uptake of anthropogenic CO_2 into the surface ocean. The third set of processes are associated with changes in the seasonal difference of the drivers, that is, the $\Delta^{\text{seas}}X$ terms owing to, for example, a change in ocean circulation/mixing or biological activity.

These terms can be grouped according to whether they act on the thermal or non-thermal components. This gives, for the thermal component,

$$\frac{d\Delta^{\text{seas}}p_{\text{CO}_2}^{\text{th}}}{dt} = \frac{\gamma_T \times \frac{dp_{\text{CO}_2}}{dt} \times \Delta^{\text{seas}}\text{SST}}{\text{change in surface } p_{\text{CO}_2}} + \frac{\gamma_T \times p_{\text{CO}_2} \times \frac{d\Delta^{\text{seas}}\text{SST}}{dt}}{\text{seasonal difference change}} \quad (11)$$

and for the non-thermal component, namely that driven by changes in sDIC,

$$\begin{aligned} \frac{d\Delta^{\text{seas}}p_{\text{CO}_2}^{\text{nt}}}{dt} = & \frac{\frac{d\gamma_{\text{DIC}}}{dt} \times \frac{p_{\text{CO}_2}}{\text{DIC}} \times \Delta^{\text{seas}}\text{sDIC}}{\text{Revelle factor change}} \\ & + \frac{\gamma_{\text{DIC}} \times \frac{dp_{\text{CO}_2}}{dt} \times \frac{d\Delta^{\text{seas}}\text{sDIC}}{\text{DIC}}}{\text{change in surface } p_{\text{CO}_2}} \\ & + \frac{\gamma_{\text{DIC}} \times \frac{p_{\text{CO}_2}}{\text{DIC}} \times \frac{d\Delta^{\text{seas}}\text{sDIC}}{dt}}{\text{seasonal difference change}} \end{aligned} \quad (12)$$

Here we quantify the impact of only the first two sets of drivers, that is, the surface ocean p_{CO_2} driven change and the change in the Revelle factor, as we currently lack good observations for the trends in $\Delta^{\text{seas}}X$ terms. Therefore, deviation between our observation-based CO_2 estimate and the theoretical framework can be partly explained by the third set of drivers (as well as by the neglected contributions from alkalinity and the freshwater balance).

We have already all the input data³⁴ to estimate the CO_2 effect for the thermal component (10), but we need to estimate the seasonal difference of sDIC required to estimate the CO_2 effect for the non-thermal component. We estimate this term, $\Delta^{\text{seas}}\text{sDIC}$, from p_{CO_2} using equation (8) and fields from the Global Data Analysis Project version 2 database^{35,36}

$$\Delta^{\text{seas}}\text{sDIC} = \left(\Delta^{\text{seas}}p_{\text{CO}_2} - \gamma_T \times p_{\text{CO}_2} \times \Delta^{\text{seas}}\text{SST} \right) \times \frac{\text{DIC}}{\gamma_{\text{DIC}} \times p_{\text{CO}_2}} \quad (13)$$

and the change in the Revelle factor as⁶

$$\frac{d\gamma_{\text{DIC}}}{dt} = \frac{d\gamma_{\text{DIC}}}{d\text{DIC}} \times \frac{p_{\text{CO}_2}/\text{DIC}}{\gamma_{\text{DIC}}} \times \frac{dp_{\text{CO}_2}^{\text{atm}}}{dt} \quad (14)$$

using the dry air mixing ratio of atmospheric CO_2 (<https://www.esrl.noaa.gov/gmd/ccgg/mbl/>) with a long-term mean $dp_{\text{CO}_2}^{\text{atm}}/dt$ of $1.7 \mu\text{atm yr}^{-1}$, and by using the approximation⁶

$$\gamma_{\text{DIC}} \approx \frac{3 \times \text{Alk} \times \text{DIC} - 2 \times \text{DIC}^2}{(2 \times \text{DIC} - \text{Alk}) \times (\text{Alk} - \text{DIC})} \quad (15)$$

we derive

$$\frac{d\gamma_{\text{DIC}}}{d\text{DIC}} = \frac{\text{Alk}^2 \times (4 \times \text{DIC} - 3 \times \text{Alk})}{(\text{DIC} - \text{Alk})^2 \times (2 \times \text{DIC} - \text{Alk})^2} \quad (16)$$

which yields the expected change in the non-thermal p_{CO_2} seasonal difference in response to a change in Revelle factor plus the oceanic accumulation of anthropogenic CO_2 . While the above approximation for the Revelle factor is far from being accurate, tests with a full model of the aqueous CO_2 system show that this approximation is reasonably close to the accurate results. We retain the approximation, given its simplicity.

The results of equations (11) and (12) as well as their combination in equation (10) are displayed in Fig. 4 as dashed green lines.

Uncertainty analysis. Two main sources of uncertainty contribute to the uncertainty of the reported trend in the winter-minus-summer difference in

surface ocean p_{CO_2} . The first source is associated with the uncertainty in the spatiotemporal interpolation of the observations, which directly affects the diagnosed magnitude of the seasonal cycle. The second source of uncertainty stems from the determination of the 34-year linear trend in the winter-minus-summer difference in the presence of interannual to decadal variations.

We use the surface ocean p_{CO_2} residuals, computed as the difference between our interpolated p_{CO_2} estimate minus the SOCATv4 gridded data¹¹, as the basis for computing the uncertainty for the winter-minus-summer difference. These residuals contain no visible temporal trends, either for the summer or for the winter season (see Supplementary Information), and do not depend on the data density. This permits us to assume that the error structure of our interpolated p_{CO_2} is stationary and random in time, and thus not biasing the determination of the linear trend. Nevertheless, the substantial residuals (root mean squared deviation of a typical magnitude of $10\text{--}20 \mu\text{atm}$) imply a considerable uncertainty of the reconstructed seasonal cycle. But as we determine the mean seasonal cycle for large spatial regions, this uncertainty of the mean, that is, the standard error of the mean, goes down with 1 over the square root of the effective sample size N^{eff} , that is,

$$\text{standard error of the mean} \approx \frac{\text{root mean squared deviation}}{\sqrt{N^{\text{eff}}}} \quad (17)$$

where N^{eff} represents the spatially decorrelated number of p_{CO_2} residuals per region. We calculate it from

$$N^{\text{eff}} \approx N \times \frac{1-r}{1+r} \quad (18)$$

where N is the total number of residuals per region and r is the lag 1 autocorrelation coefficient. We estimate r by randomly plotting the squared difference of the p_{CO_2} residuals as a function of haversine distance. We do this for five randomly chosen and non-repeating subsamples of 1,000 residual pairs each, binning them into 300 km bins and calculating

$$r = \frac{\sum_{d=1}^{n-1} (x_d - \langle x_{1:n-1} \rangle)(x_{d+1} - \langle x_{2:n} \rangle)}{\left(\sum_{d=1}^{n-1} (x_d - \langle x_{1:n-1} \rangle)^2 \right)^{1/2} \left(\sum_{d=1}^{n-1} (x_{d+1} - \langle x_{2:n} \rangle)^2 \right)^{1/2}} \quad (19)$$

where x is the residual difference squared of two locations separated by the distance d , and $\langle x \rangle$ represents the average squared distance. The standard error of the mean is computed for each analysis region.

To determine the uncertainty of the linear trend in the annual winter-minus-summer differences for each of the regions, we take the 95% confidence interval reported in the output of the least-squares regression fit in MATLAB. We test whether the trends are significantly different from 0 using standard t -statistics.

Data availability. Our p_{CO_2} analysis is based on measurements extracted from the SOCATv4¹¹, freely available via <https://www.socat.info>. The neural-network-based interpolated sea surface p_{CO_2} product used in this study is freely accessible at the National Centers for Environmental Information via https://www.nodc.noaa.gov/oceans/SPCO2_1982_2015_ETH_SOM_FFN.html. We further use bottle data from the Bermuda Atlantic Time-series Study¹⁶ and from the closely located Hydrostation 'S'¹⁵ to compute the surface ocean p_{CO_2} at these two sites near Bermuda. These data are available online via <http://bats.bios.edu>. For the Hawaiian Ocean Time-series station¹⁴, we extracted the already computed p_{CO_2} data from http://hahana.soest.hawaii.edu/hot/products/HOT_surface_CO2.txt. Additionally, for our calculations, we use the gridded product from the Global Data Analysis Project version 2^{35,37}, which can be freely accessed from <https://www.nodc.noaa.gov/oceans/GLODAPv2/>, and the National Oceanic and Atmospheric Administration's Earth System Research Laboratory marine boundary layer reference dry air mixing ratio of atmospheric CO_2 , freely accessed from <https://www.esrl.noaa.gov/gmd/ccgg/mbl/>. Lastly, we use the National Oceanic and Atmospheric Administration's Optimum Interpolation version 2³⁴ SST product, freely accessed via <https://www.esrl.noaa.gov/psd/data/gridded/data.noaa.oisst.v2.html>, for our calculations.

References

- Craven, H. D. et al. Enhanced seasonal exchange of CO_2 by northern ecosystems since 1960. *Science* **341**, 1085–1089 (2013).
- Lovenduski, N. S., Gruber, N., Doney, S. C. & Lima, D. I. Enhanced CO_2 outgassing in the Southern Ocean from a positive phase of the Southern Annular Mode. *Glob. Biogeochem. Cycles* **21**, GB2026 (2007).
- Zeebe, P. E. & Wolf-Gladrow, D. *CO_2 in Seawater: Equilibrium, Kinetics, Isotopes* (Elsevier, Amsterdam, 2001).
- Lee, K. et al. Global relationships of total alkalinity with salinity and temperature in surface waters of the world's oceans. *Geophys. Res. Lett.* **33**, L19605 (2006).

34. Reynolds, R. W., Rayner, N. A., Smith, T. M., Stokes, D. C. & Wang, W. An improved in situ and satellite SST analysis for climate. *J. Clim.* **15**, 1609–1625 (2002).
35. Lauvset, S. K. et al. A new global interior ocean mapped climatology: the 1°×1° GLODAP version 2. *Earth Syst. Sci. Data* **8**, 325–340 (2016).
36. Olsen, A. et al. The Global Ocean Data Analysis Project version 2 (GLODAPv2)—an internally consistent data product for the world ocean. *Earth Syst. Sci. Data* **8**, 297–323 (2016).
37. Key, R. et al. *Global Ocean Data Analysis Project version 2 (GLODAPv2)*, ORNL/CDIAC-162, ND-P093 (Carbon Dioxide Information Analysis Center, 2015), https://doi.org/10.3334/CDIAC/OTG.NDP093_GLODAPv2.